INSTITUTE OF PHYSICS PUBLISHING SMART MATERIALS AND STRUCTURES
Smart Mater. Struct. **11** (2002) 288–296 PII: S0964-1726(02)34308-8

Harmonic analysis of a magnetorheological damper for vibration control

W H Liao[1] **and C Y Lai**

Smart Materials and Structures Laboratory, Department of Automation and Computer-Aided Engineering, The Chinese University of Hong Kong, Shatin, NT, Hong Kong

E-mail: whliao@cuhk.edu.hk

Received 21 November 2001, in final form 11 February 2002
Published 5 April 2002
Online at stacks.iop.org/SMS/11/288

Abstract
Semi-active control systems are becoming more popular because they offer both the reliability of passive systems and the versatility of active control systems without imposing heavy power demands. In particular, it has been found that magnetorheological (MR) fluids can be designed to be very effective vibration control actuators, which use MR fluids to produce controllable damping force. The objective of this paper is to study a single-degree-of-freedom (SDOF) isolation system with an MR fluid damper under harmonic excitations. A mathematical model of the MR fluid damper with experimental verification is adopted. The motion characteristics of the SDOF system with the MR damper are studied and compared with those of the system with a conventional viscous damper. The energy dissipated and equivalent damping coefficient of the MR damper in terms of input voltage, displacement amplitude and frequency are investigated. The relative displacement with respect to the base excitation is also quantified and compared with that of the conventional viscous damper through updating the equivalent damping coefficient with changing driving frequency. In addition, the transmissibility of the MR damper system with semi-active control is also discussed. The results of this study are valuable for understanding the characteristics of the MR damper to provide effective damping for the purpose of vibration isolation or suppression.

(Some figures in this article are in colour only in the electronic version)

1. Introduction

Isolation or suspension systems can be used to control the vibration of moving systems. To reduce the system vibration, effective vibration control of the isolation or suspension systems is necessary. Vibration control techniques have classically been categorized into two areas, namely, passive and active controls. In a passive system, the parameters are synthesized through off-line design techniques and no on-line feedback actions are used. Since passive systems produce fixed designs, the control would not be optimal when the system or the operating condition changed. On the other hand, active controls have been of popular interest in recent years. Force or torque inputs from actuators are usually used to suppress vibration amplitudes based on on-line measurements from sensors. The advantage of an active approach is that it can adapt for system variations, and can be much more effective than passive systems. Considering the above two methods, one can see the merit of combining the feedback concept in active systems with adaptable energy dissipation devices whose damping/stiffness characteristics can be varied according to the control commands. This semi-active control approach has been investigated by several researchers [1–4]. It has advantages over passive systems for better performance and it requires less power than active control.

In particular, it has been found that magnetorheological (MR) fluids can be quite promising for vibration reduction

[1] Author to whom any correspondence should be addressed.

applications [5]. MR fluids are magnetic analogs of electrorheological (ER) fluids and typically consist of micrometre-sized, magnetically polarizable particles dispersed in a carrier medium such as mineral or silicone oil. When a magnetic field is applied to the fluid, particle chains form, and the fluid becomes a semi-solid and exhibits viscoplastic behaviour similar to that of ER fluid. This controllable change of state with some desirable features such as high strength, good stability, broad operational temperature range and fast response time gives rise to isolation and suspension system applications. MR fluid dampers considered here are semi-active control devices that use MR fluids to produce controllable damping forces.

Recently, semi-active vibration systems via ER/MR fluid dampers have been discussed by some researchers. A sliding mode control algorithm was developed by Wang *et al* [2] to maximize the damping effects of ER fluid dampers for structural vibration control. An experimental approach was made to seismic protection through MR dampers by Dyke *et al* [6]. The hysteresis behaviour of the linear stroke MR damper was characterized by four different models [7]. Also, a viscoelastic–plastic model was considered by Li *et al* [8] to model an MR damper. An alternative representation of an MR damper in terms of neural network was developed by Chang and Roschke [9]. A seat suspension system, equipped with a skyhook control scheme, using an MR damper has been developed by Choi *et al* [10].

2. Problem statement and objective

While the previous studies on MR dampers have shown promising results, it should be noted that the MR dampers either in passive-on or semi-active controlled modes could be further explored as compared with systems with conventional viscous dampers. The goal of this research is to investigate the characteristics of the MR damper and a single-degree-of-freedom (SDOF) system with the MR damper through experimental studies and analyses under harmonic excitation of the base. In particular, it will be explained why the frequency shift of the peak transmissibility for the MR damper system is different from that with the viscous damper. The transmissibility will also be quantified and compared with that of the conventional viscous damper through updating the equivalent damping coefficient with changing driving frequency. These issues will be thoroughly addressed in this study.

3. MR damper behavior and modeling

3.1. MR damper and model

The MR damper used in this study is RD-1005-1, which was manufactured by Lord Corporation. The length of the damper is 20.83 cm in its extended position. It has a 5 cm stroke. The maximum current to the electromagnet in the magnetic choke is 2 A and the coil resistance is 5Ω.

To evaluate the performance of MR dampers in vibration control applications and to take full advantage of the unique features of these devices, a model is needed to accurately describe the behaviour of the MR damper. The mathematical model proposed by Spencer *et al* [11] is adopted in this study.

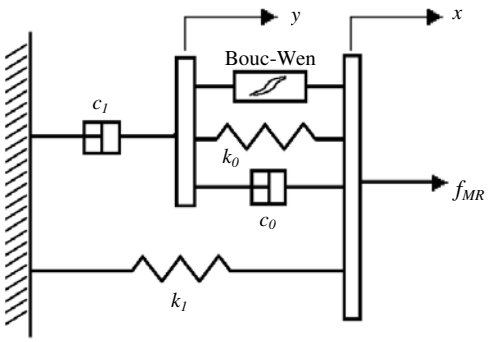

Figure 1. Mechanical model of the MR damper.

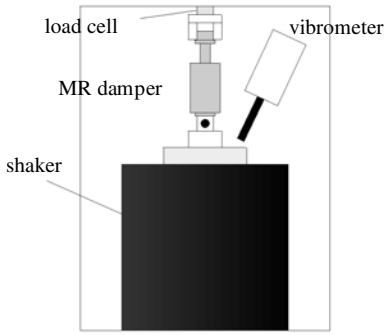

Figure 2. Schematic test setup for the MR damper.

The hysteretic behaviour in the damper was described by the Bouc–Wen model. The mechanical realization of the MR damper is shown in figure 1. The phenomenological model is governed by the following equations [11]:

$$\dot{y} = \frac{1}{(c_0 + c_1)}[\alpha z + k_0(x - y) + c_0\dot{x}] \tag{1}$$

$$\dot{z} = -\gamma|\dot{x} - \dot{y}||z|^{n-1}z - \mu(\dot{x} - \dot{y})|z|^n + A(\dot{x} - \dot{y}) \tag{2}$$

$$f_{MR} = c_1\dot{y} + k_1(x - x_0) \tag{3}$$

$$\alpha = \alpha(u) = \alpha_a + \alpha_b u \tag{4}$$

$$c_1 = c_1(u) = c_{1a} + c_{1b}u \tag{5}$$

$$c_0 = c_0(u) = c_{0a} + c_{0b}u \tag{6}$$

$$\dot{u} = -\eta(u - v) \tag{7}$$

where v is the voltage applied to the current driver. In this model, there are a total of 14 parameters $(c_{0a}, c_{0b}, k_0, c_{1a}, c_{1b}, k_1, x_0, \alpha_a, \alpha_b, \gamma, \mu, A, n, \eta)$ to characterize the MR damper. The optimized values for the 14 parameters are determined by fitting the model to the experimental data obtained.

3.2. Experimental setup

The load frame shown in figure 2 is set up and built for the purpose of obtaining MR damper response data for parameter identification. The dynamic responses of the damper can be measured for prescribed waveforms and frequencies. The vibration system (Labworks Inc., LW-127-500) is used to

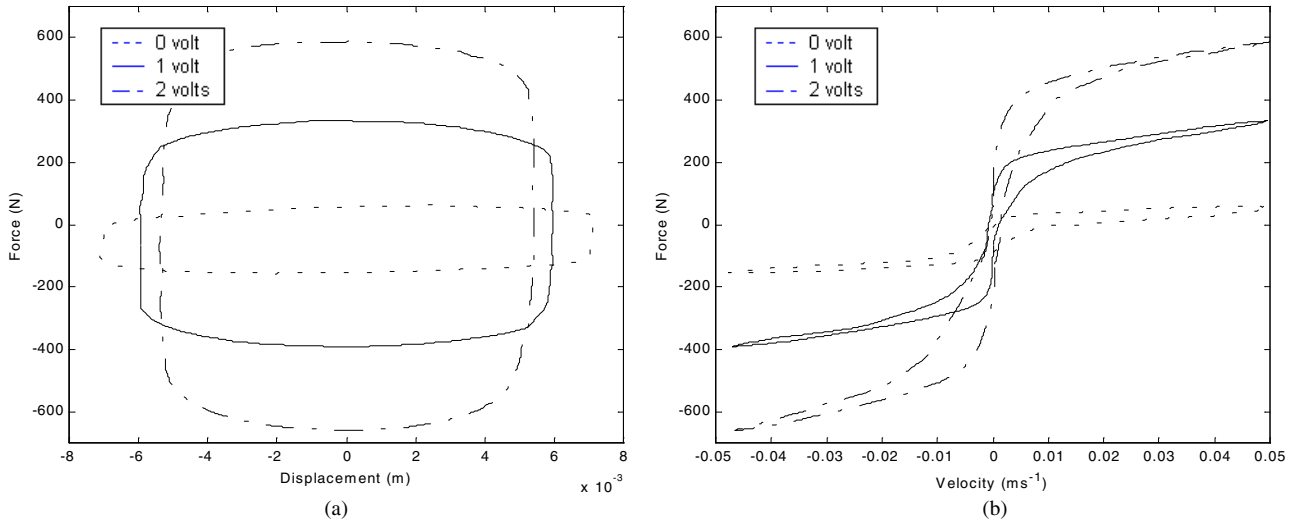

Figure 3. Force versus displacement and velocity of the MR damper. (*a*) Force–displacement relationship. (*b*) Force–velocity relationship.

produce excitation for the damper. It consists of a shaker (ET-127) and a matching power amplifier (PA-123-3/2-500). The amplifier receives an electrical signal, amplifies it and sends it to the shaker. The load cell (PCB Piezotronics Inc., 208C03) can sense the damping force under different conditions. A laser vibrometer (Polytec GMBH, OFV-3001) is used to measure the related displacement and velocity.

In order to acquire the experimental data (displacement, velocity and damping force of the MR damper), the dSPACE system is used. It also commands a suitable voltage signal to the MR damper. The dSPACE system consists of two main elements—software and hardware. The software interfaces with MATLAB on a PC and allows the user to create a block diagram of the system in Simulink. The dSPACE real-time interface, which runs under MATLAB, can then compile the Simulink model and load the model directly to a DSP chip in the hardware of the dSPACE system. The hardware portion consists of the DSP processor board. All data for this research were acquired directly using the TRACE module in the dSPACE toolkit. TRACE can generate a time history of any variable in the Simulink control block diagram.

3.3. Damper characteristics

In this experiment, the shaker is driven with a sinusoidal signal with a fixed frequency, and the voltage applied to the damper is held at a constant level. Three sets of experimental data are obtained according to three voltage levels (0, 1, and 2 V). Each set of data consists of displacement, velocity and damping force. The responses of the MR damper subject to a 1 Hz sinusoidal signal are shown in figure 3 for three constant voltage levels applied to the damper. Both force–displacement and force–velocity loops are shown in the figure. The force–displacement loops (figure 3(*a*)) progress along a clockwise path with the increase of time while the force–velocity loops (figure 3(*b*)) progress along a counterclockwise path. Also, it can be seen that, as the voltage increases, the corresponding damping force increases.

Observing both figures 3(*a*) and (*b*), the force produced by the damper is not centered at zero. This shows the effect of the accumulator at the bottom of the damper. Also, the maximum force increases with increasing applied voltage, which is related to the magnetic field.

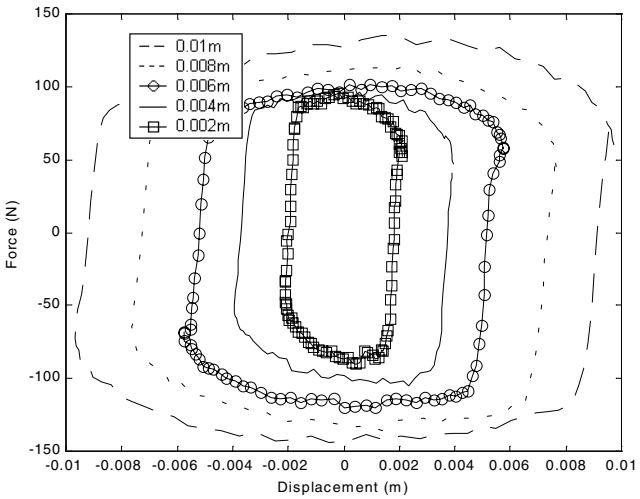

Figure 4. Force–displacement relation with different excitation amplitudes.

As shown in figure 3(*b*), when the damping force is less than the yield force, the damper is operating in the pre-yield region. It strongly exhibits hysteresis characteristics. Also, the slope of the curve is relatively steep. When the damping force is larger than the yield force, the damper is operating in the post-yield region. The yield transition occurs as the damping force crosses the yield force value. After the yield force values, the change rate of damping force with velocity is relatively low.

In order to compare the damping performance of the MR damper with that of a conventional viscous damper, an equivalent damping coefficient c_{eq} is determined by equating the energy dissipated in a full cycle [7, 8]. In the following experiments, sinusoidal excitations with different amplitudes are used to test the characteristics under different constant voltages. For example, with no voltage input, five sets of data (peak amplitudes of excitations are 0.002, 0.004, 0.006, 0.008 and 0.01 m), under 1 Hz excitation, are captured and five sets of force versus displacement curves are shown in

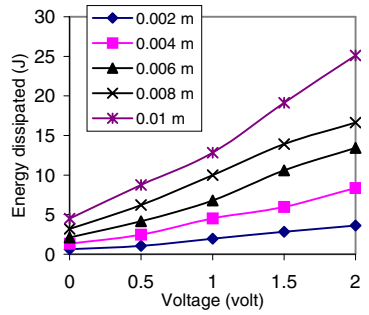

Figure 5. Energy dissipated versus voltage.

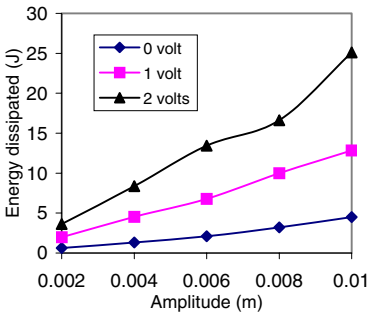

Figure 6. Energy dissipated versus displacement amplitude.

figure 4. In a similar way, some experiments are performed under sinusoidal excitations with different frequencies (0.2, 0.6, 1, 1.4 and 1.8 Hz) with fixed excitation amplitude.

Let the energy dissipated by the MR damper in one cycle be W

$$W = \int_0^{2\pi/\omega_d} f_{MR}\,\mathrm{d}x = \int_0^{2\pi/\omega_d} c_{eq}\dot{x}\,\mathrm{d}x \qquad (8)$$

where ω_d is the driving frequency of the sinusoidal excitation, $\dot{x}$ is the relative velocity of the damper and f_{MR} is the measured damping force.

It should be noted that W can be found from the area enclosed by the curve in the force–displacement diagram under a particular voltage input, excitation amplitude and frequency. Then, the energy dissipated per cycle in each case can be calculated. The relations among W, input voltage, excitation amplitude and frequency are shown in figures 5–7. The excitation frequency for the results shown in figures 5 and 6 is 1 Hz. For figure 7, while the excitation amplitude is kept constant (0.004 m peak-to-peak), the excitation frequency and voltage input are to be varied. From figure 4, it is obvious that a greater energy dissipated results from a greater excitation amplitude due to a larger loop. Also, for higher voltage input, the loop will be larger due to the higher damping force. This results in a larger amount of energy dissipated. These results are also shown in figures 5 and 6.

Observing figure 7, for the same voltage input, the variance of the energy dissipated under the excitation of higher frequency is less than that under lower-frequency excitation. This shows that, at higher frequencies, the energy dissipated varies little with the excitation frequency for a fixed amplitude. As mentioned before, the energy can be found from the area enclosed by the force–displacement loop, such as those in figure 4. For the MR damper, the force–displacement loop is in a rectangular-like shape, so the area of the loop can be

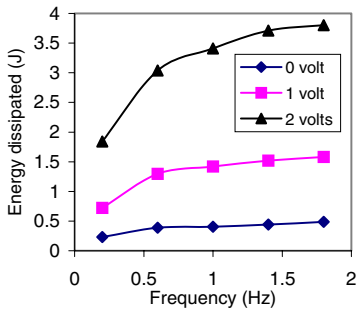

Figure 7. Energy dissipated versus frequency.

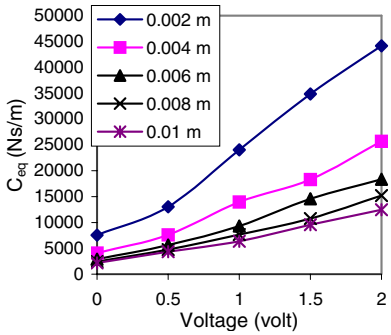

Figure 8. Equivalent damping coefficient versus input voltage.

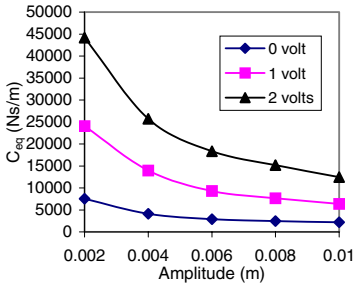

Figure 9. Equivalent damping coefficient versus displacement amplitude.

estimated by the product of the peak-to-peak value of the displacement and that of the damping force. For a fixed excitation amplitude, since it has been shown that the energy dissipated varies little with the frequency for higher-frequency excitation, the peak-to-peak value of the damping force also varies little. This means that, at higher frequencies, the excitation frequency does not affect the damping force much for a fixed amplitude.

From equation (8), assuming a simple harmonic excitation, $x(t) = X\sin\omega_d t$, where X is the amplitude of the relative motion of the damper,

$$W = \int_0^{2\pi/\omega_d} c_{eq}(\dot{x})^2\,\mathrm{d}t$$
$$= \int_0^{2\pi/\omega_d} c_{eq}(\omega_d X\cos\omega_d t)^2\,\mathrm{d}t = \pi c_{eq}\omega_d X^2. \qquad (9)$$

Therefore, c_{eq} can be found as

$$c_{eq} = \frac{W}{\pi\omega_d X^2}. \qquad (10)$$

The relations among c_{eq}, input voltage, excitation amplitude and frequency are shown in figures 8–10. The

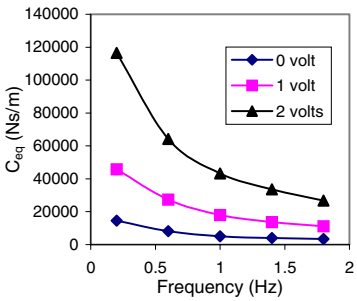

Figure 10. Equivalent damping coefficient versus frequency.

damping coefficients in figures 8–10 correspond to the energy dissipated shown in figures 5–7, respectively. Figure 8 shows that the damping coefficient increases with the increase of the input voltage for a constant-amplitude input. Also, for the amount of increment in c_{eq}, the effect of the increase in voltage on lower amplitudes is more significant than that on higher amplitudes. This shows that the value of the damping coefficient changes dramatically with applied voltage at a low amplitude where the velocity is relatively low for a fixed frequency. For higher velocities, when the displacement amplitude is higher, the change in c_{eq} with the voltage is less significant.

In figure 9, it can be seen that the damping coefficient decreases as the excitation amplitude is raised under the same input voltage. For the same amount of increment in displacement amplitude, the damping coefficient for the higher voltage input decreases more. Compared with figure 6, which shows that energy dissipated increases with the excitation amplitude, it is interesting to see that the trend for c_{eq} is opposite to that for the energy dissipated with the same voltage input. This is because, from equation (10), c_{eq} is treated as a normalized damping factor for the amount of dissipated energy with respect to excitation frequency and amplitude. From equation (10), for c_{eq}, W is divided by the square of X. Therefore, for the approximately linear increase of W with X in figure 6, c_{eq} decreases with the increase of X.

In figure 10, when the displacement (0.004 m peak-to-peak) is kept fixed, an increase in frequency leads to a decrease in damping coefficient. The amount of reduction is larger for higher voltage input. This can be explained by the effect of the pre-yield/post-yield phase. For lower excitation frequencies, a smaller velocity will result at the same excitation amplitude. Then, the damper operates in the pre-yield region. From figure 3(*b*), when the fluid in the damper is in the pre-yield phase, the slope of the curve is relatively steep compared with that in the post-yield phase. Basically, the slope can reflect the damping ability, which is described quantitatively by the equivalent damping coefficient. When the velocity is increased, the damper would work beyond the pre-yield region. In the post-yield region, the slope of curve in figure 3(*b*) is much smaller. Therefore, on average, the damping coefficient of the MR damper working at higher frequencies is smaller.

3.4. Comparison between model and experimental data

In order to obtain the optimized parameters for the MR damper model from the above experimental data, a least-squares optimization method is used. The optimization is performed using the function 'leastsq' available in MATLAB. The 14 parameters are estimated by minimizing the error between the model-predicted force (f_{model}) and the force from experimental results ($f_{\text{experiment}}$). The error concerned is represented by the objective function J, which is given by

$$J = \sum (f_{\text{experiment}} - f_{\text{model}})^2. \tag{11}$$

It should be noted that the number of points for calculation is 400 and the sampling time is 0.005 s. The resulting parameters are given in table 1.

Table 1. Parameters for the model.

Parameter	Value	Parameter	Value
c_{0a}	784 N s m^{-1}	α_a	12 441 N m^{-1}
c_{0b}	1803 N s V^{-1} m^{-1}	α_b	38 430 N V^{-1}m^{-1}
k_0	3610 N m^{-1}	γ	136 320 m^{-2}
c_{1a}	14 649 N s m^{-1}	μ	2059 020 m^{-2}
c_{1b}	34 622 N s V^{-1} m^{-1}	A	58
k_1	840 N m^{-1}	n	2
x_0	0.0245 m	η	190 s^{-1}

Figure 11 shows the comparison of the predicted model with the experimental data for five constant voltages (0, 0.5, 1, 1.5 and 2 V). It can be seen that the model accurately predicts the behaviour of the damper.

4. Vibration characteristics of a base-excited system

Consider an SDOF isolation system with base excitation shown in figure 12; the equation of motion is

$$m_s\ddot{x}_s + c(\dot{x}_s - \dot{x}_b) + k(x_s - x_b) = 0 \tag{12}$$

where m_s is the system mass, $x_s, \dot{x}_s$ are the vertical displacement and velocity of the mass, k is the stiffness coefficient, $x_b, \dot{x}_b$ are the displacement and velocity of the base and c is the damping coefficient.

By replacing the viscous damper with an MR damper, the SDOF isolation system with the MR damper is shown in figure 13. The governing equation of motion is

$$m_s\ddot{x}_s + k(x_s - x_b) + f_{MR} = 0 \tag{13}$$

where f_{MR} is the controllable damping force.

4.1. SDOF system with viscous damper

Considering the SDOF system with a viscous damper (figure 12), assume the base of the system undergoes harmonic motion, i.e.

$$x_b(t) = X_b \sin \omega t. \tag{14}$$

Then the system response can be expressed as $x_s(t) = X_s \sin(\omega t - \phi)$. The displacement transmissibility amplitude X_s/X_b and phase angle ϕ can be obtained as

$$\frac{X_s}{X_b} = \left[\frac{k^2 + (c\omega)^2}{(k - m_s\omega^2)^2 + (c\omega)^2}\right]^{\frac{1}{2}} = \left[\frac{1 + (2\zeta r)^2}{(1 - r^2)^2 + (2\zeta r)^2}\right]^{\frac{1}{2}} \tag{15}$$

$$\phi = \tan^{-1}\left[\frac{2\zeta r^3}{1 + (4\zeta^2 - 1)r^2}\right] \tag{16}$$

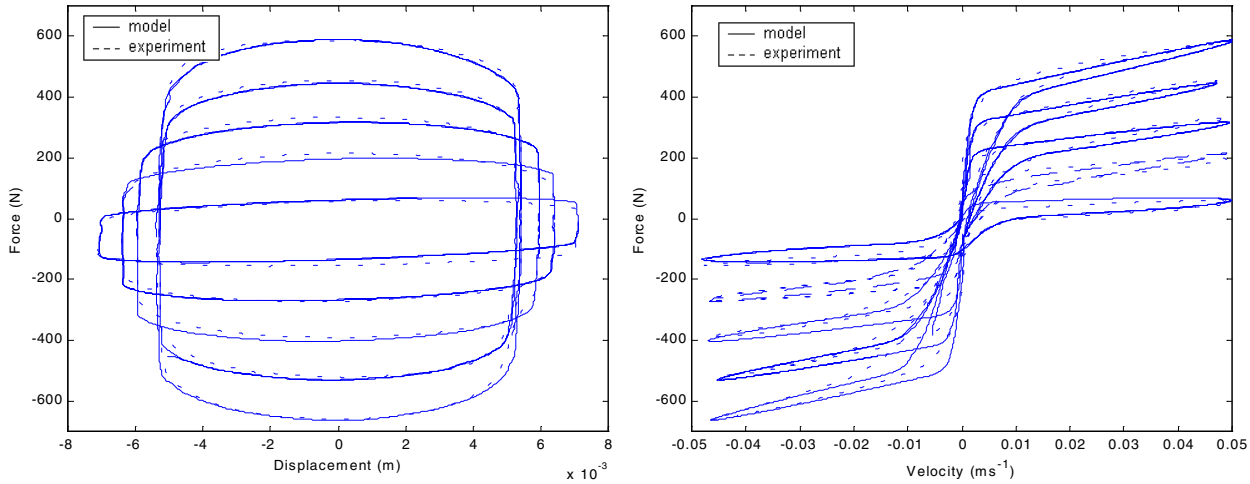

Figure 11. Comparison of model and experimental results. (*a*) Force–displacement relationship. (*b*) Force–velocity relationship.

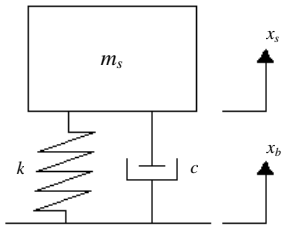

Figure 12. SDOF system with viscous damper.

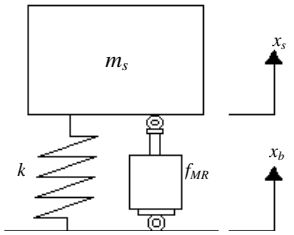

Figure 13. SDOF system with MR damper.

where $\zeta = c/2\sqrt{m_s k}$ and $r = \omega/\omega_n = \omega\sqrt{m_s}/\sqrt{k}$; ω_n is the natural frequency of the system. ζ is the damping ratio and r is the frequency ratio.

The displacement transmissibility and the phase angle of the SDOF system, where all the elements of the system are passive, are shown in figure 14 for various damping coefficients. From figure 14(*a*), it can be seen that at low passive damping the maximum transmissibility (at resonance) is relatively large, while the transmissibility at higher frequency is low.

As the damping is increased, the resonance peak is attenuated but isolation is lost at high frequency. This transmissibility plot illustrates the inherent tradeoff between resonance control and high-frequency isolation that is associated with the design of passive isolation system. Also, from figure 14(*a*), the location of the peak of the transmissibility for the damping ratio 0.2 is almost at unit frequency ratio. However, as the damping ratio is increased, the location of the peak shifts to smaller frequency ratios. Figure 14(*b*) presents the coupling effect between the base excitation and the motion of the system mass. A small phase angle means that the two ends of the damper are strongly coupled and are moving in phase with each other. Increasing damping causes more coupling across the isolation system.

4.2. SDOF system with passive MR damper

Using the MR damper model studied in section 3, the displacement transmissibility and phase angle can be found through simulation.

In the simulation, the system mass is set to be 1500 kg and the stiffness of the spring is 75 000 N m^{-1}. The amplitude of the base excitation is set to be 0.01 m. The results are shown in figure 15. As expected, they are similar to those cases with the viscous damper. Around the resonance frequency, the transmissibility is high for low damping (low voltage applied). In this case, 0 V input causes the lowest damping of the MR damper. As the voltage applied is increased, the transmissibility decreases. For higher frequencies ($r > 1.5$), lower voltage input (lower damping) has better isolation.

One interesting thing to note is that the location of the peak of the transmissibility shifts to higher frequency ratios as the input voltage increases (larger damping). This is totally different from the case with the viscous damper. In order to investigate this characteristic, the corresponding equivalent damping coefficient c_{eq} has to be found. Before determining the energy dissipated in one cycle, the amplitude of relative motion $(x_s - x_b)$ of the damper for the SDOF system should be found. The relative displacements of the damper are shown in figure 16.

By using equation (10), c_{eq} can be calculated by substituting X by the relative displacement where W can be found by using equation (8). The plot of this value against frequency ratio for various input voltages is shown in figure 17. The displacement transmissibility can be calculated using equation (15) by varying damping and frequency. These results are plotted in figure 18 with the results from figure 15(*a*) for the purpose of comparison. It can be seen that the transmissibility from the system simulation is quite close to that calculated from c_{eq}.

In figure 17, the equivalent damping coefficients drop for all voltage cases as the frequency ratio increases although the

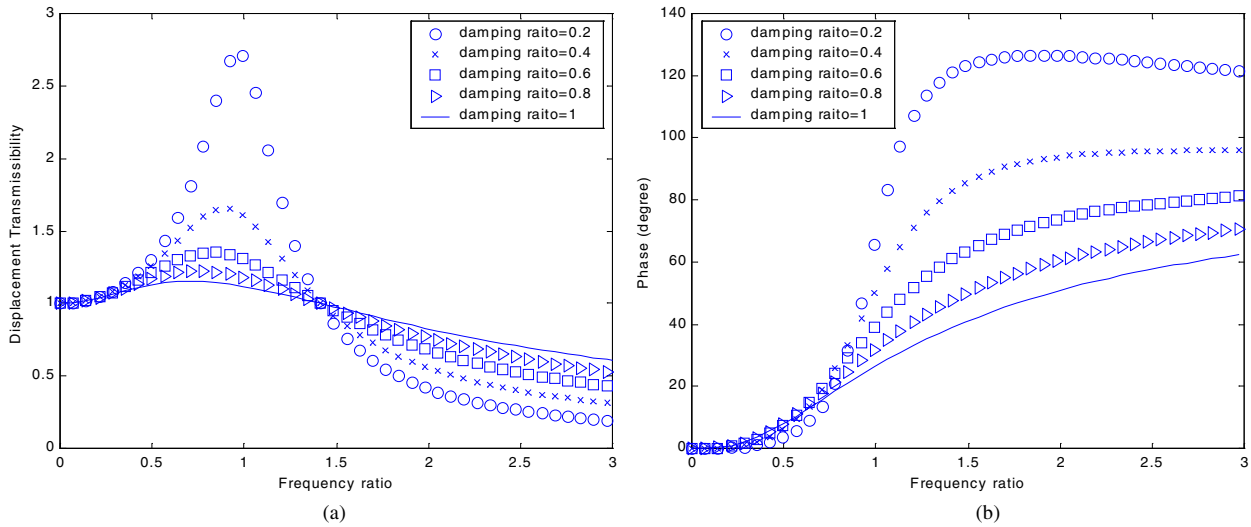

Figure 14. Transmissibility and phase for the passive system with viscous damper. (*a*) Displacement transmissibility. (*b*) Phase angle.

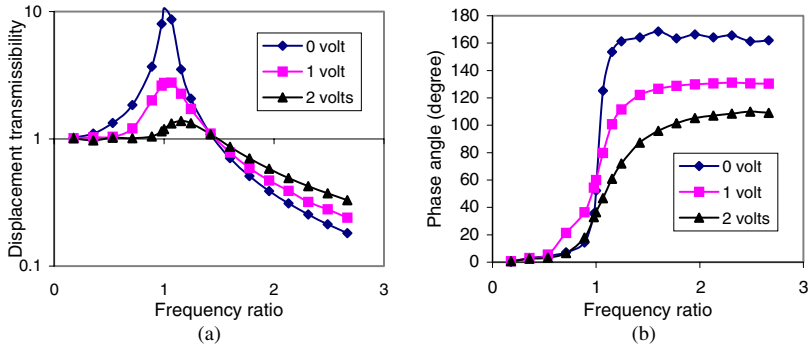

Figure 15. Transmissibility and phase for the passive system with MR damper. (*a*) Displacement transmissibility. (*b*) Phase angle.

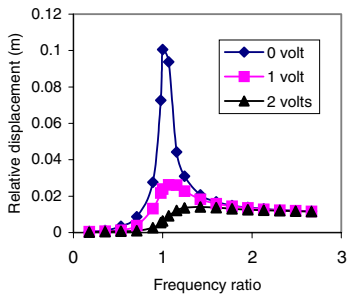

Figure 16. Relative displacement of the SDOF system with MR damper.

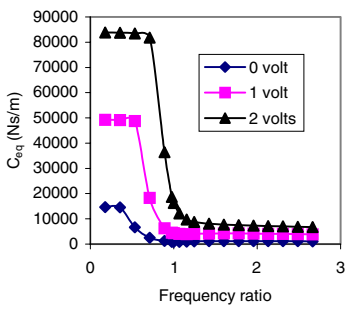

Figure 17. Equivalent damping coefficient for the passive system with MR damper.

locations of the drops are different. Referring to figure 16, when c_{eq} remains at a high value, the amplitude of relative displacement is low. This means that the MR fluid in the damper is near pre-yield phase at this time. When the amplitude of relative displacement is higher, the damping force exceeds the yield force of the MR fluid and the damper operates in the post-yield region. In this phase, the equivalent damping will be much smaller. This illustrates that c_{eq} can change dramatically with the amplitude of the relative displacement.

In figure 17, the c_{eq} value drops significantly from the frequency ratio of about 0.8 for 2 V input while it drops from that of about 0.4 for 0 V input. That is, for the 0 V case, the coefficient starts to drop at lower frequency ratios. Then, for 2 V, c_{eq} drops to as low as 9000 N s m^{-1} after the unit frequency ratio and it stays at that level afterwards. However, for 0 V, it can reach the steady value of c_{eq} at around the unit frequency ratio. It is obvious that c_{eq} for 2 V starts to decrease late (in the sense of frequency ratio) and reaches the steady value late. In figure 15(*a*), the transmissibility for 2 V input therefore starts to increase at the frequency ratio of about 0.8 and it will not reach the peak at the unit frequency ratio. It will have a peak after the unit frequency ratio as there still exists a significant drop of c_{eq} for the 2 V case at the unit frequency ratio. From figure 14(*a*), it should be reminded that the transmissibility at resonance increases significantly with the decrease of damping. This is why a sudden damping drop can increase the transmissibility.

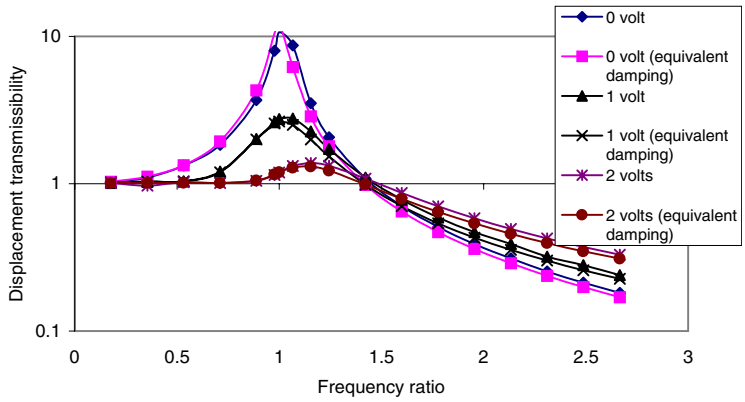

Figure 18. Comparison between two transmissibilities of the SDOF system.

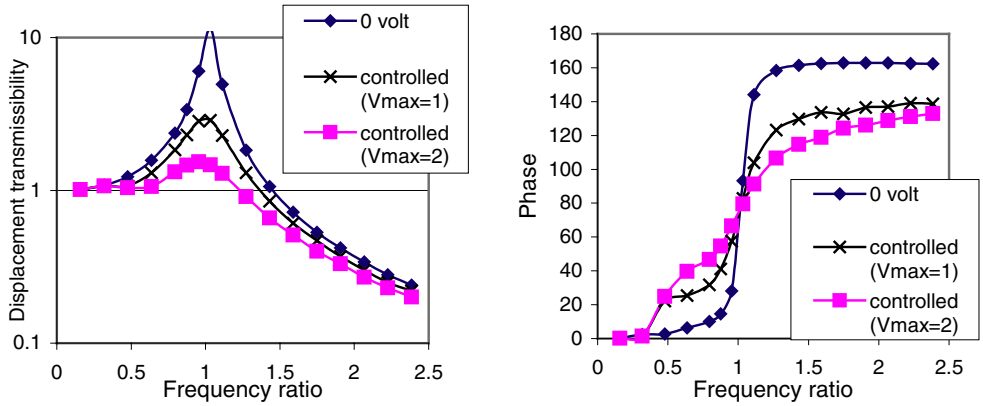

(a) (b)

Figure 19. Transmissibility and phase of the controlled system. (*a*) Displacement transmissibility. (*b*) Phase angle.

4.3. SDOF system with semi-active MR damper

In this section, the performance of the semi-active vibration control of the SDOF MR system is evaluated through the transmissibility analysis. With the consideration of the loading uncertainties, the sliding mode control is used for the system controller. The sliding surface is defined as

$$S = \dot{e} + \lambda e \tag{17}$$

where

$$e = x_s - x_{ref}. \tag{18}$$

The reference model used here is the ideal skyhook system, which has been reported to be highly effective in controlling a one-degree-of-freedom system [12]. For loading perturbation, $m_s = m_{so} + \Delta m_s$ where m_{so} represents the nominal mass and Δm_s is the uncertain part. The desired control force f_d can be derived as [13]

$$f_d = -m_{so}[u_o' - K' \operatorname{sgn}(S)] \tag{19}$$

where

$$u_o' = \left(\frac{k}{m_{so}}x_s - \frac{k}{m_{so}}x_b - \lambda\dot{e} + \ddot{x}_{ref}\right) \tag{20}$$

$$K' = \beta\left[\left(1 - \frac{1}{\beta}\right)\left(\frac{k}{m_{so}}|x_s| + \frac{k}{m_{so}}|x_o| + |u_o'|\right) + \varphi\right]. \tag{21}$$

It should be noted that the MR damper is a semi-active device, which cannot generate force arbitrarily as an active actuator. Therefore, a continuous state controller can be used to deal with the semi-active MR damper [14]. The algorithm for selecting the command signal is stated as

if

$$G(f_d - Bf_{MR}) \operatorname{sgn}(f_{MR}) > V_{\max}$$
$$v = V_{\max}$$

else if

$$G(f_d - Bf_{MR}) \operatorname{sgn}(f_{MR}) < V_{\min} \tag{22}$$
$$v = V_{\min}$$

else

$$v = G(f_d - Bf_{MR}) \operatorname{sgn}(f_{MR})$$

where $V_{\max}$ is the maximum voltage to the damper and $V_{\min}$ is the minimum voltage to the damper (i.e. 0 V).

The nominal parameters used in this study are $m_{so} = 1500$ kg, $k = 75\,000$ N m^{-1} and $\Delta m_s = -300$ kg. The damping coefficient (c_{ref}) of the reference model is 35 000 N sm^{-1}. λ, β and φ are chosen to be 4, 1.25 and 2, respectively, while the values of G and B are set to be 0.021 and 1, respectively. In figure 19, there are two controlled cases with the maximum voltage to the MR damper bounded by 1 or 2 V. In both cases, it can be seen that the isolation performances of the controlled systems are better than that of the system with no voltage applied. This shows that the semi-active controller

with the MR damper is quite effective for suppressing vibration for the whole frequency range shown. This is different from the tradeoff phenomena of the passive systems, where worse isolation was obtained for higher frequencies while increasing the damping (see sections 4.1 and 4.2). Comparing these two controlled cases, one should note that the displacement transmissibility of the controlled system with maximum 2 V to the damper is lower than that with the maximum voltage set to 1 V. Observing figure 19(*b*), the phase plot also shows a key difference, where the semi-active controlled case with larger maximum voltage to the MR damper has larger phase angles for lower frequencies (frequency ratio < 1) but smaller phase angles for higher frequencies (frequency ratio > 1).

5. Conclusion

The application of an MR fluid damper for the vibration control of an SDOF system is studied. First, the characteristics of the MR damper are investigated, and some experiments on the damper are performed. Then, a mathematical model of the MR fluid damper is adopted. The parameters for the model are successfully estimated from experimental data. The energy dissipated and equivalent damping coefficient of the MR damper in terms of input voltage, displacement amplitude and frequency are investigated. The SDOF isolation system with the MR damper is analyzed by studying its transmissibility. Also, the relative displacement with respect to the base excitation is quantified and compared with that of the conventional viscous damper by updating the equivalent damping coefficient with changing driving frequency. Some interesting observations are obtained and their physical insights are explained. In addition, the performance of the MR damper system with semi-active control is also discussed. Compared with passive systems, the results of this study show that the semi-active controlled MR damper can achieve effective vibration suppression without the sacrifice of worse isolation for higher frequencies of interest.

Acknowledgment

The work described in this paper was supported by a grant from the Research Grants Council of Hong Kong Special Administrative Region, China (project no CUHK4216/01E).

References

[1] Kim Y S, Wang K W and Lee H S 1992 Feedback control of ER-fluid-based structures for vibration suppression *Smart Mater. Struct.* **1** 139–45

[2] Wang K W, Kim Y S and Shea D B 1994 Structural vibration control via electrorheological-fluid-based actuators with adaptive viscous and frictional damping *J. Sound Vib.* **177** 227–37

[3] Taniwangsa W and Kelly J M 1997 Experimental testing of a semi-active control scheme for vibration suppression *Proc. SPIE Conf. on Smart Structures and Materials: Passive Damping and Isolation (SPIE vol 3045)* (Bellingham, WA: SPIE) pp 130–9

[4] Sadek F and Mohraz B 1998 Semiactive control algorithms for structures with variable dampers *J. Eng. Mech.* **124** 981–90

[5] Dyke S J, Spencer B F Jr, Sain M K and Carlson J D 1996 Modelling and control of magnetorheological dampers for seismic response reduction *Smart Mater. Struct.* **5** 565–75

[6] Dyke S J, Spencer B F Jr, Sain M K and Carlson J D 1998 An experimental study of MR dampers for seismic protection *Smart Mater. Struct.* **7** 693–703

[7] Wereley N M, Pang L and Kamath G M 1998 Idealized hysteresis modeling of electrorheological and magnetorheological dampers *J. Intell. Mater. Syst. Struct.* **9** 642–9

[8] Li W H, Yao G Z, Chen G, Yeo S H and Yap F F 2000 Testing and steady state modeling of a linear MR damper under sinusoidal loading *Smart Mater. Struct.* **9** 95–102

[9] Chang C C and Roschke P 1998 Neural network modeling of a magnetorheological damper *J. Intell. Mater. Syst. Struct.* **9** 755–64

[10] Choi S B, Nam M H and Lee B K 2000 Vibration control of a MR seat damper for commercial vehicles *J. Intell. Mater. Syst. Struct.* **11** 936–44

[11] Spencer B F Jr, Dyke S J, Sain M K and Carlson J D 1997 Phenomenological model of a magnetorheological damper *J. Eng. Mech.* **123** 230–8

[12] Ahmadian M 1999 On the isolation properties of semiactive dampers *J. Vib. Control* **5** 217–32

[13] Lai C Y and Liao W H Vibration control of a suspension system via a magnetorheological fluid damper *J. Vib. Control* at press

[14] Sims N D, Stanway R, Peel D J, Bullough W A and Johnson A R 1999 Controllable viscous damping: an experimental study of an electrorheological long-stroke damper under proportional feedback control *Smart Mater. Struct.* **8** 601–15